The Astronomical Journal, 166:212 (12pp), 2023 November https://doi.org/10.3847/1538-3881/acfef5

The Cycles of Alpha Centauri: Double Dipping of AB

Thomas Ayres
Center for Astrophysics and Space Astronomy, 389 UCB, University of Colorado, Boulder, CO 80309, USA; Thomas.Ayres@Colorado.edu
Received 2023 August 8; revised 2023 September 20; accepted 2023 September 29; published 2023 November 1

Abstract

In mid-2023, the Sunlike dwarfs of nearby α Centauri (HD 128620 ("A"): G2 V; HD 128621 ("B"): K1 V; hereafter "AB") coincidentally both entered coronal ($T \approx 1$–3 MK) low states in their long-term X-ray cycles, as captured by the Chandra Observatory and its High Resolution Camera (HRC-I). The assessment benefited from a sensitivity degradation model for HRC-I based on a "check star," the F subgiant Procyon (α Canis Minoris A; HD 61421: F5 IV–V), further validated by Hubble Space Telescope time series of the Fe XII 1241.985 Å and 1349.396 Å coronal forbidden lines ($T \approx 1.6$ MK) of all three stars. The AB starspot-cycle periods noted previously, 19 and 8 yr, appear to be holding. These deviate substantially from the 11 yr solar example, despite only modest differences in the stellar properties. The new cycle-minimum L_X/L_{BOL} of α Cen A is similar to that of the previous minimum observed by Chandra in 2005–2010, and close to solar-MIN X-ray levels in 2009 and 2019, with implications for the "basal" coronal flux of low-activity early G stars. The recent α Cen B X-ray MIN is similar to that in 2016 but higher than an earlier one in 2007–2009. Significantly, the B X-ray minima (in L_X/L_{BOL}) are comparable to the solar Cycle 24 maximum, suggesting plentiful starspots at the B-cycle MIN (contrary to the solar case). Tangentially, the current AB low states favor Doppler-reflex detections of planets, as opposed to the coronal high states, when elevated chromospheric activity can add nuisance signals to radial velocity time series.

Unified Astronomy Thesaurus concepts: X-ray telescopes (1825); Single x-ray stars (1461); Ultraviolet spectroscopy (2284); Ultraviolet sources (1741); Ultraviolet telescopes (1743); Starspots (1572); Solar cycle (1487)

1. Introduction

The Alpha Centauri AB binary has routinely been imaged by Chandra X-ray Observatory with its High-Resolution Camera (HRC-I), roughly every 6 months from late 2005 to the present. The Chandra program overlapped a prior monitoring campaign carried out by XMM-Newton using its European Photon Imaging Camera (EPIC, with pn and MOS CCD modules), started in 2003 (Robrade et al. 2005; Robrade et al. 2012). There were even earlier X-ray efforts during the 1990s by the ROSAT High Resolution Imager[1] (Schmitt & Liefke 2004). The objective of these several projects has been to follow the high-energy evolution of long-term coronal ($T \approx 1$–3 MK) cycles of the two nearby ($d = 1.34$ pc) stars, as additional, accessible examples of the phenomenon beyond the well-studied case of the Sun itself. The latter is famous for its 11 yr ebb and flow of sunspots, although in reality the underlying magnetic cycle is double that when alternating polarity reversals of the global field are counted. The solar cycling has been attributed to a deep-seated magnetic "dynamo" (Parker 1970), whose generative power arises from an interplay between (differential) rotation and convection, and which induces a back-and-forth competition between large-scale internal poloidal and toroidal fields, leading to regular outbreaks of surface activity on the decadal schedule (e.g., Babcock 1961; Leighton 1969).

A compelling motivation to investigate the roto-convective dynamo is that violent eruptions on the Sun powered by the magnetic activity are at the root of heliospheric "space weather" (SW). The associated high-energy X-ray radiation, energetic particles, and plasma ejections can impact the planets of the solar system, especially technology-laden Earth with its unique vulnerabilities. Beyond the Sun, analogs of SW from host stars can cause photochemical damage and erosion of exoplanet atmospheres, potentially hostile to the genesis and survival of life (Airapetian et al. 2020). X-ray observations are an essential tool to explore stellar activity because the high-energy emissions have a vastly stronger response to magnetic-related atmospheric heating than lower-temperature species like the famous chromospheric Ca II H and K lines (near 3950 Å; Wilson 1978), the ground-based mainstays of such efforts prior to the space age.

The following is a progress report on the recent behavior of the X-ray cycles of α Cen AB. In mid-2023, A and B coincidentally both entered coronal low states, a relatively uncommon occurrence. This has implications, among other things, for assessing the "basal" coronal emissions at starspot cycle minima, improving knowledge of the cycle periods, and peripherally for detecting planetary companions around these very nearby stars. The recognition of the double X-ray dimming was thanks to Chandra HRC-I, which unfortunately was mostly out of commission for more than a year because of technical issues, but recently is back in service. The project also benefited from far-ultraviolet (FUV: 1150–1700 Å) measurements by Hubble Space Telescope's (HST) Space Telescope Imaging Spectrograph (STIS) to validate a proposed sensitivity decline of Chandra HRC-I over the past several years.

[1] A microchannel-plate-intensified solid-state detector that was a forerunner of the Chandra HRC-I.

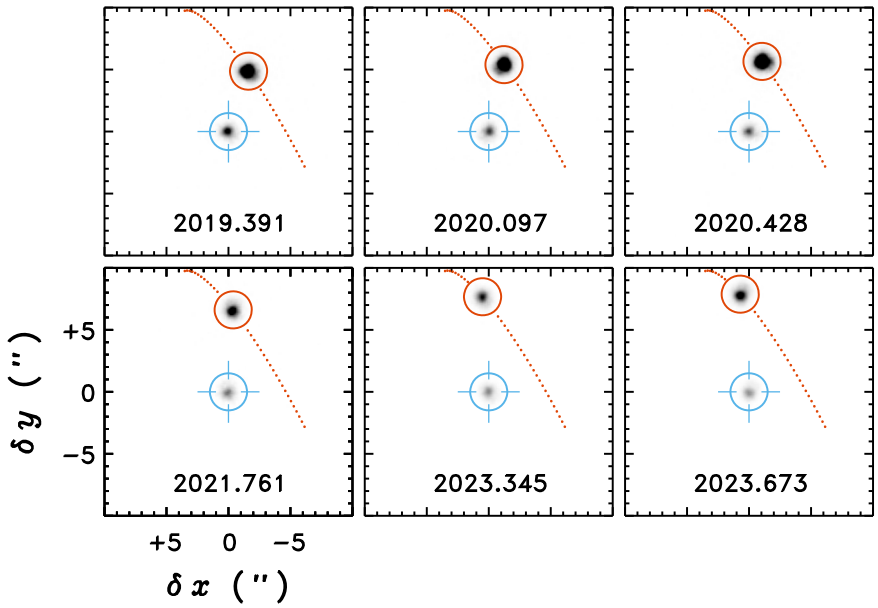

Figure 1. Recent Chandra HRC-I images of α Cen AB. North is up, east to the left. The snapshots share the same reverse gray scale for the intensities (counts s^{-1} $pixel^{-1}$). The x- and y-axes are relative sky coordinates, centered on the primary star (A; blue cross-hairs). The secondary (B) is circled in red. Dotted curves indicate the orbital path of B: note the increasing AB separation in recent years.

2. Recent Chandra X-Ray Observations

Chandra and its HRC-I camera have important advantages for observing X-ray-luminous and visually bright stars like α Cen, as summarized by Ayres (2009, hereafter A09). HRC-I is not affected by "pileup" for sources with a high count rate (CR), is relatively immune to "optical loading" for visually bright objects, and the 1″ imaging of Chandra easily resolves the α Cen binary, especially during 2013–2019, when the AB separation in the 80 yr orbit slipped below 6″, impacting lower-resolution XMM-Newton. A downside of HRC-I is lack of energy discrimination compared to the CCD-type detectors. However, the conversion factor to translate an HRC-I CR to an absolute flux can be optimized through emission measure modeling (see Ayres & Buzasi 2022, hereafter AB22). Thus, HRC-I is a valuable coronal irradiance photometer for Sunlike stars.

Figure 1 illustrates recent Chandra HRC-I pointings on α Cen AB. The images were derived from the level-2 event lists and preserve the native 1″ resolution. The intensities are in counts per second per spatial pixel. The reverse gray scales are the same for each snapshot. The x- and y-axes are sky coordinates in arcseconds, relative to the primary star (A; blue cross-hairs). The secondary (B) is circled in red. The $r = 1.''5$ circles represent the adopted 95% encircled energy detection cell. Red-dotted curves trace the orbital path of B relative to A (Akeson et al. 2021), from 2010 (lower right) to 2030 (upper left). The UT date of the pointing is listed in each panel.

Within this series, the maximum CR of A was 0.8 counts s^{-1} (top left panel), the minimum was 0.3 (bottom right panel), the maximum of B was 3.9 (top right panel), and the minimum was 0.8 (bottom middle panel). Both A and B have faded in apparent CR since 2020.

The 2021 observation is a concatenation of two 5 ks exposures that, owing to an earlier postponed pointing, were doubled up to maintain the desired 6-month cadence (see Ayres 2022a). The time gap between the bottom left and bottom middle panels was caused by a pause of HRC-I operations in early 2022 to resolve sporadic electronic issues. The camera was returned to service in 2023 April.

There were two recent HRC-I observations of AB (ObsID 25497: 2023 May 6; ObsID 25498: 2023 September 3) acquired after the Ayres (2021, hereafter A21) and AB22 summaries of X-ray measurements of AB and the F-type subgiant Procyon. The latter was crucial to the present study because, despite a moderately high X-ray luminosity, Procyon appears to be remarkably constant in its high-energy emissions (A21) and thus can potentially serve as an instrumental-sensitivity "check star." There also was a more recent HRC-I pointing on Procyon (ObsID 25503: 2023 May 5), about a day and a half before one of the new observations of α Cen.

There are a few Chandra HRC-S exposures of AB and Procyon, mainly zeroth-order images from the Low-Energy Transmission Grating Spectrometer (LETGS). Here, just the HRC-I observations were considered, to avoid possible systematic errors devolving from uncertainties in the relative calibration of the very different modes. Both AB and Procyon are visually too bright to be imaged with Chandra's ACIS energy-resolving CCD cameras, which lack suitable blocking filters to suppress the excessive optical loading.

HRC-I CRs of α Cen AB and Procyon were determined as follows:

1. The apparent source location was found by centroiding the respective event cloud from the entire observation of a given epoch.
2. Time-stamped events were collected in an $r = 1.''5$ detection cell (95% encircled energy) centered on the source.
3. The detection cell photon list was divided into 250 s segments. Counts were summed for each temporal bin and then divided by the dead-time-corrected exposure of that bin.
4. An estimated cosmic background for each time segment was inferred from the counts in an annulus 30″–100″ centered on the source, scaled back to the size of the

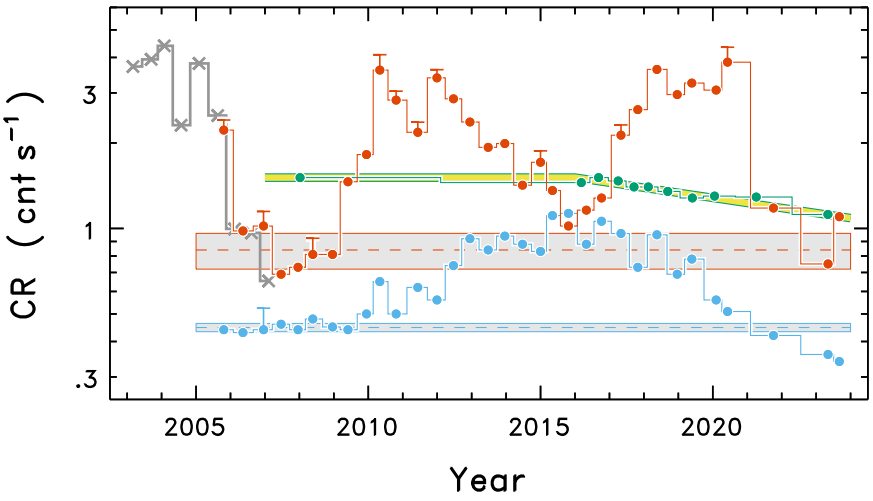

Figure 2. Time series of Chandra HRC-I CRs of α Cen A (blue filled circles), α Cen B (red), and Procyon (green). One-sided error bars (from the flare-filtering method) indicate degree of variability where significant. Gray crosses to the left are averages of XMM-Newton CRs of B, scaled to HRC-I. The slanted yellow line corresponds to a decline of 3.5% per year post-2016 for Procyon.

detection cell. The background corrections were negligible in all cases, however, given the bright coronal sources, short time segments, and small cell size.

5. The time series of binned CRs for the specific observation (typically 20–40 samples) was subjected to an "Olympic filter," which removed the lowest 15% and highest 15% of the points and calculated an average CR from the surviving values. Tests have shown that this simple, symmetric elimination successfully suppresses most transient flare enhancements (more conspicuous in more active B). The scheme works because the most common type of flare is a weak, short-lived event (1 ks or less), whereas the typical observation is long (5–10 ks). Consequently, any CR upticks normally span only a modest fraction of the exposure duration and will naturally occupy the upper intensity bins ultimately discarded by the Olympic filter. Because the elimination scheme is symmetric, it preserves the average CR in the situation of a constant source with randomly distributed fluctuations (say, due to counting statistics).
6. The final step was to correct the HRC-I CRs for the 95% encircled energy factor.

A metric was devised to flag the occurrence of short-term flux enhancements. A standard deviation was calculated for each epoch relative to the filtered "quiescent" CR by considering all the bins in the time sequence and then dividing by the Poisson uncertainty (in counts s^{-1}) of the 250 s time step based on the quiescent CR. The rounded ratio will be unity for a constant source modulated by Poisson fluctuations. However, if there was a transient flare or a gradient of CR during the pointing (e.g., a long-duration flare decay), the rounded ratio ("s") will exceed 1. As seen in Table A1, only one of the A observations (out of 33) had $s > 1$, whereas 10 observations of the (more active) B component bested that limit (the highest s value was 4). Further, none of the 11 Procyon epochs in Table A2 had $s > 1$.

Figure 2 illustrates the derived CRs for α Cen A (blue filled circles), α Cen B (red), and Procyon (green), in the post-2000 Chandra/XMM-Newton era. Gray crosses, 2003–2007, are averages of XMM-Newton pn and MOS1 CRs of B (from A09) scaled to HRC-I in the overlapping time range. XMM-Newton measurements of α Cen A were not included, because the thick blocking filter used to mitigate optical loading for visually bright AB strongly suppresses the soft response of the EPIC modules, which adversely affects the CR of A, especially during its coronal low states (A09). One-sided error bars indicate the degree of variability of the unfiltered time series for those pointings with $s \geqslant 2$. Formal Poisson uncertainties of the flare-filtered average CRs are smaller than the symbol sizes (<2%), due to the large number of counts in the retained 70% of each observation.

The thin gray horizontal stripe for A represents the average CR and standard deviation for 2005.5–2009.5, an extended X-ray minimum in the long-term coronal activity cycle. The broader gray band is similar for B over the (albeit more volatile) low state, 2006.0–2009.0. The initially flat and then downward-slanted yellow line for Procyon suggests a trend of decreasing HRC-I sensitivity post-2016 (note, however, that there is only the single X-ray point for Procyon prior to 2016). Note also that both A and B have recent CRs that are similar to or below the historical minima prior to 2010.

3. X-Ray Analysis

The apparent decline of the Procyon CRs since 2016 suggests a sensitivity decrease of $\delta \approx 3.5$ % yr^{-1}, when defined as

$$\mathrm{CR_{OBS}} = \mathrm{CR_{TRUE}} \times (1 - \delta\,[(t - 2016) > 0]), \qquad (1)$$

where t is the observation date in years and the expression in square brackets is understood to be zero for $t \leqslant 2016$.

A corresponding correction (inverse of the parenthetical expression above) was applied to the CR time series of the three stars. Absolute fluxes at Earth, f_X (erg cm^{-2} s^{-1}), were then derived from the corrected CRs using the approach described by AB22. This involved an optimization scheme applied to each observation, based on a grid of coronal emission measure distribution (EMD) models developed by Wood et al. (2018) from Chandra LETGS spectra of 19 representative late-type dwarf stars, including α Cen AB of this study. The adopted energy range is 0.1–2.4 keV (ROSAT "PSPC standard band"). Examples of the modeling can be found in AB22.

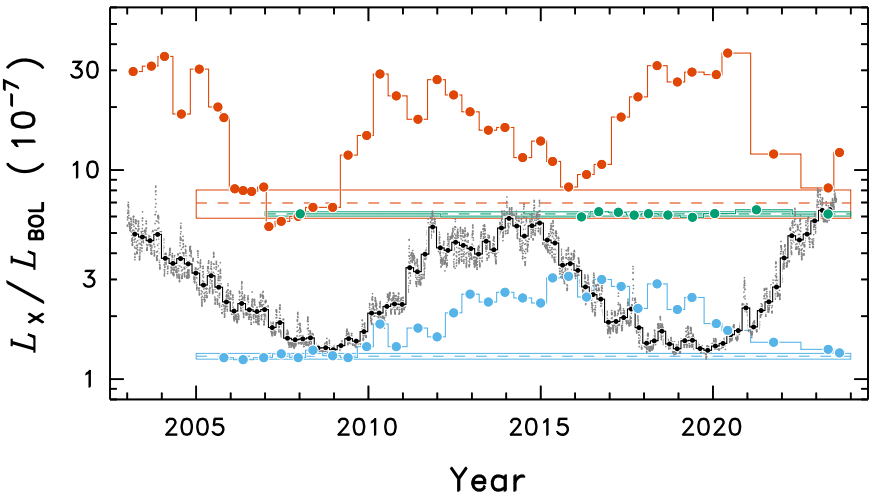

Figure 3. Time series of sensitivity-corrected, calibrated X-ray fluxes (0.1–2.4 keV) of α Cen AB and Procyon (same color-coding as in Figure 2), expressed as L_X/L_{BOL}. Small gray points represent daily solar X-ray irradiances over the declining phase of sunspot Cycle 23 (left side), the whole of Cycle 24 (middle), and the rise of current Cycle 25 (right side). Black filled circles are 81-day averages (three rotations).

A valuable property of HRC-I is that the energy conversion factor (ECF) does not depend strongly on the EMD models for these types of soft coronal sources. The uncorrected CRs and derived fluxes are reported in Appendix A. The CRs and fluxes differ slightly from previous tabulations (e.g., Ayres 2014, hereafter A14; A21; AB22), due to the implementation here of a simpler flare filter and ongoing refinements of the AB22 optimization algorithm. The calibrated fluxes also benefited from better knowledge of the (proposed) HRC-I sensitivity trend.

Figure 3 depicts time series of bolometrically normalized X-ray luminosities of α Cen AB and Procyon. The scaled XMM-Newton CRs of B prior to 2007 were interleaved with the HRC-I values in time order and calibrated in the same way. The bolometric normalization debiases, to some extent, for the different stellar distances and sizes, allowing a fairer comparison. The f_{BOL} values were taken from A21.[2] The blue, red, and green outlined horizontal stripes highlight reference cycle minimum levels, as in Figure 2. Now, with the proposed HRC-I sensitivity correction, the recent low normalized X-ray luminosities of both A and B are better aligned with the previous cycle minima. The small gray dots are daily averages of the solar X-ray spectral irradiance taken from the FISM2[3] database, integrated over the 0.1–2.4 keV reference band and expressed as L_X/L_{BOL}. Black filled circles are 81 days averages (three solar rotations).

It appears that α Cen A and B are coincidentally entering coronal low states at the same time. The double dipping has observational consequences that will be described later. At least that is the picture if the proposed sensitivity decline of HRC-I is correct. Alternatively, if the camera response has, for example, remained constant since 2016, then α Cen A is entering a deeper coronal minimum than has been seen historically, and Procyon—a type of star not known for coronal cycling—is experiencing an unprecedented long-term decline.

A deeper-than-usual starspot minimum of near-solar-twin α Cen A could inform the question of what the high-energy solar cycle might have been like prior to the direct measurements of the present spacecraft era. Notably, several hundred years ago, during a prolonged period in the seventeenth century called the Maunder Minimum, sunspots were rarely seen and, coincidentally or not, Northern Europe was caught in the throes of a "Little Ice Age" (Eddy 1976). The cycle minimum of the Sun and similar low-activity stars like α Cen A should represent a state when there are few or no dynamo spots or associated plage regions on the stellar surface. The residual high-energy FUV and X-ray emissions would then arise from processes that are present at all phases of the cycle but disconnected from the dynamo oscillation itself. Examples are chromospheric shock waves associated with photospheric *p*-modes (e.g., Rutten & Uitenbroek 1991; Carlsson & Stein 1992) and the diminutive magnetic elements of the supergranulation pattern, which are thought to arise from a purely convective "local" or "small-scale" dynamo (e.g., Rempel et al. 2023, and references to previous work therein). However, if the low-state high-energy emissions are not invariable, but rather differ from cycle to cycle, then there must be more to the "basal" emission-level story.

Under these circumstances, it is conceivable that the Maunder Minimum Sun might have experienced much reduced supergranulation activity, a collateral reduction in high-energy emissions, and possible subtle side effects on the solar irradiance itself, with repercussions for Earth's climate (e.g., Judge et al. 2012; Yeo et al. 2020; Liu et al. 2023). The historic (i.e., pre-1970s) X-ray emissions of the Sun are inaccessible, so the only recourse is to examine the behavior of other Sunlike stars, such as α Cen A of the present study, to test for violations of the constancy of coronal low states. This is a prime example of the so-called solar–stellar connection.

Unfortunately, Chandra has no suitable radiometric calibration sources that mimic the energy distributions of low-activity coronal stars, to confirm the apparent HRC-I sensitivity decline suggested by Procyon. Further, any sensitivity variation of the HRC-I camera could well be energy dependent, so it might not be revealed by the harder X-ray sources normally monitored for the purpose. There is a way out of the dilemma, however, that involves FUV spectra from HST.

[2] $L_X/L_{BOL} = f_X/f_{BOL}$, where in practice the second expression is the one that is calculated explicitly (from the apparent fluxes, *f*; see AB22).
[3] See https://lasp.colorado.edu/lisird/data/fism_daily_hr.

4. HST FUV Observations

A possible way to independently corroborate the X-ray behavior of the program stars capitalizes on a pair of forbidden lines of Fe XII, 1241 and 1349,[4] hot coronal interlopers, as it were, in the otherwise lower-temperature ultraviolet landscape (see, e.g., Ayres et al. 2003). Fe^{+11} is a member of the phosphorus isoelectronic sequence, and its main resonance lines, 3*p*–4*s* and 3*p*–4*d*, fall in the ultrasoft X-ray band below 90 Å. The FUV magnetic dipole transitions connect a pair of low-lying excited levels, $3s^2\ 3p^3\ ^2P^o_{1/2,3/2}$ to the $3s^2\ 3p^3\ ^4S^o_{3/2}$ ground state. The Astrophysical Plasma Emission Database (APED)[5] emissivity curves of these coronal transitions peak at 1.6 MK and have a temperature dependence that roughly matches the EMDs of α Cen B and Procyon, as well as α Cen A at the maximum of its long-term activity cycle (α Cen A sheds the hotter components of its EMD during coronal low states; see A14). For this reason, the FUV Fe XII forbidden lines can potentially serve as a proxy for the coronal X-rays, at least for these relatively soft sources. However, the Fe XII emissions are faint, so care must be exercised to obtain spectra with an adequate signal-to-noise ratio (S/N) and to be wary of accidental blends that might affect the line strengths.

Helpfully, there is an extensive time-domain collection of FUV exposures of α Cen AB and Procyon, obtained with high-precision HST/STIS in a series of loosely coordinated campaigns jointly with Chandra since 2010. All three stars are bright in the FUV, mainly due to proximity to Earth, and deliver high S/N in short HST visits. The most relevant FUV spectra were acquired after the repair of STIS in Hubble Servicing Mission 4 (SM4; 2009). Post-SM4, α Cen A has been observed exclusively with the STIS medium-resolution echelle, E140M-1425, and the $0\farcs2 \times 0\farcs2$ "photometric" aperture, to achieve good resolution ($\lambda/\Delta\lambda \approx 4 \times 10^4$) and high throughput. That combination was used for many of the observations of α Cen B and Procyon as well.

However, there were several epochs when the high-resolution STIS echelle E140H was employed for those two stars, again with the $0\farcs2 \times 0\farcs2$ slot to achieve optimum sensitivity. The native 1.1×10^5 resolution is slightly degraded with the photometric aperture, but still more than twice E140M. A pair of CENWAVEs, 1307 and 1489, were deployed to span the range 1206–1590 Å, which encompasses most of the important FUV spectral features. The E140H option was chosen for α Cen B because the FUV features of the K dwarf are narrower than those of the warmer stars (A21), whereas E140H was justified for Procyon, despite its generally broader lines, on the basis of elevated FUV brightness and a rich spectrum of sharp interstellar absorptions. As a rule, higher-precision E140H is preferred over E140M, if signal levels allow for the multiple H CENWAVEs needed to cover the same spectral territory as the single M 1425 setting.

All the suitable echellegrams were de-archived from MAST en masse via the on-the-fly calibration facility to ensure the most recent reference files. The majority of the STIS FUV observations of the three stars were previously cataloged by A21. Three additional visits to α Cen AB (E140Ms for both stars) were carried out more recently. Unfortunately, there are not any newer STIS pointings on Procyon. The post-2022 STIS spectra of AB are described in Appendix B.

Initial postprocessing of the pipeline data sets included an enhanced wavelength correction (Ayres 2022b); coaddition of subexposures, if any; and merging the two CENWAVEs for the E140H visits. The methods are summarized in A21. The outcome was a set of broad-coverage FUV spectra of the three program stars over the numerous observation epochs.

In addition to the time-domain sample, all the available FUV spectra were combined to yield the highest-S/N tracings possible for each star, to fully characterize the spectral environs of the faint Fe XII coronal proxies. As mentioned earlier, the post-SM4 data sets of α Cen A were exclusively M-resolution. The nearly two dozen M spectra were interpolated onto a common wavelength scale, after registering against the leading spectrum by cross-correlation, using the narrow, bright chromospheric Cl I 1351 emission line. The spectra were then averaged, weighting by the inverse square of the wavelength-dependent photometric errors.

The data sets of α Cen B and Procyon were a mix of M and H echellegrams. The main focus of the present study was on observations through the $0\farcs2 \times 0\farcs2$ photometric aperture, because the radiometric calibration is more reliable than that of the narrow "spectroscopic" slits ($0\farcs2 \times 0\farcs06$ for E140M; $0\farcs2 \times 0\farcs09$ for E140H). The effective throughput of the thin slits can be affected by image defocusing caused by telescope "breathing" (variable thermal flexing of the Optical Telescope Assembly). All of the post-2010 STIS observations of α Cen B were with the photometric slot, but there is a group of narrow-slit STIS FUV observations of Procyon acquired in 2011 as part of a survey of late-type stars by the Advanced Spectral Library Project (ASTRAL).[6] In that group were five E140H-1271 exposures, which cover the range 1160–1360 Å and thus captured both Fe XII features. There also were five E140M-1425 exposures, one of which was through the photometric slot and the other four through the spectroscopic slit. Although not considered reliable for tracking long-term changes in the absolute FUV fluxes, the narrow-slit echellegrams can still be incorporated in the high-S/N epoch-average spectrum, because the coaddition and merging scheme accounts for variable throughputs and ultimately bootstraps a unified flux scale.

The various CENWAVEs of the two resolution groups, M and H, of α Cen B and Procyon were separately coadded, as described above for the M spectra of α Cen A, to yield an epoch average for each setting (and star). The M and several H epoch-average tracings were then merged, retaining the M spectrum for intervals lacking H coverage, and combining M and the H's for the range 1160–1590 Å, where there was joint coverage. The merging process is described in the documentation of the ASTRAL Project mentioned earlier.

A nuance is that where M and H spectra overlapped in wavelength, the M tracing was interpolated to H dispersion and filtered with the H line-spread function (LSF), while the H spectrum was filtered with the M LSF. The combined spectrum thus has a convolved LSF with slightly lower resolution (about 37,000) than M alone, but adequate for the purpose (the coronal lines are fully resolved, thanks in part to their large thermal widths). The dual M + H filtering avoids the awkward line shapes that would result from simply combining the different-resolution spectra.

[4] Hereafter, numerical values of transition wavelengths (in vacuum) are understood to be in Å.

[5] See http://atomdb.org/

[6] See https://casa.colorado.edu/~ayres/ASTRAL/

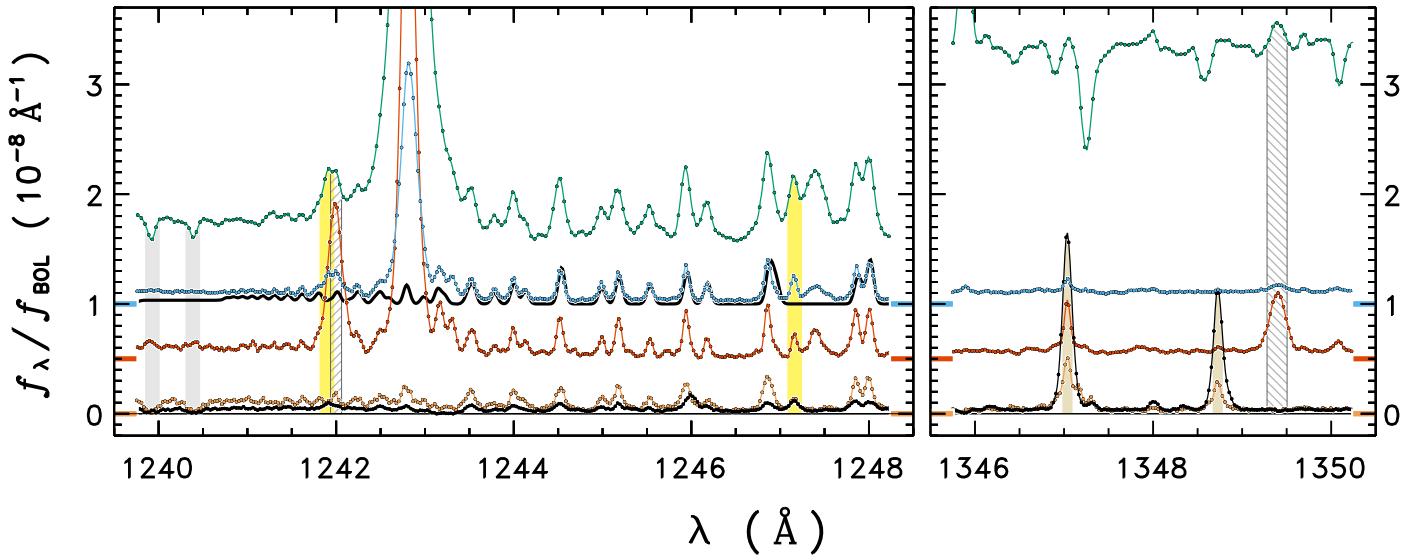

Figure 4. FUV spectral landscape of the Fe XII coronal forbidden lines. The left panel is for 1241; the right panel is for 1349. The coronal lines are hatched. The *y*-axis is the bolometrically normalized flux density. Five stars are in the comparison: Procyon (upper, green), α Cen A (middle, blue), α Cen B (lower middle, red), and the noncoronal red giants α Boo (K1 III; lower, orange) and γ Cru (M3 III; lower, black). The (shifted) zero-points of α Cen A and Procyon are thick blue tick marks at either side of the panels, those for α Boo and γ Cru are thick orange, and the α Cen B zero-point is red. The black curve in the left panel, partly covered by the α Cen A tracing, is a simulation of the C I recombination spectrum (same zero-point as A). Shaded vertical bands in both panels highlight incidental emission (and absorption) lines. The strong (unmarked) feature at 1242.8 Å is the longward component of hot subcoronal N V, weak or absent in the two red giants.

Figure 4 illustrates the twin FUV spectral intervals containing the Fe XII coronal forbidden lines. The main program stars, shifted along the *y*-axis for clarity, are marked as follows: Procyon (upper, green), α Cen A (middle, blue), and α Cen B (lower middle, red). In addition, two reference red giants were included: α Boo (K1 III; lower, orange) and γ Cru (M3 III; lower, black). The two evolved stars are "noncoronal" (severely underluminous in kilovolt X-rays; e.g., Ayres 2018 for α Boo) but display a rich spectrum of atomic and singly ionized species characteristic of the cooler chromospheric layers ($T \lesssim 10^4$ K), so they are helpful for identifying blends at the locations of the two coronal lines. Bolometric fluxes of the red giants were taken from Ayres (2023). Selected archival STIS FUV spectra of the cool giants were processed, coadded, and merged as described above for the main program stars. The (shifted) zero-points of α Cen A and Procyon are the same (thick blue tick marks at either side of the panels), as are those of α Boo and γ Cru (thick orange, at $f_\lambda/f_{BOL} = 0$). The α Cen B zero-point is red.

The strong, unmarked emission feature in the left panel is the long-wavelength component of the N V 1238 + 1242 doublet (2×10^5 K), a hot subcoronal species that is weak, if detectable at all, in the two red giants. N V 1242 is broad enough in subgiant Procyon to impose a sloping background at Fe XII 1241, which must be taken into account when fitting the coronal line (A21).

The black undulating curve in the left panel, partly covered by the α Cen A tracing, is a simple, optically thin model of the radiative recombination into the low-lying ($E = 10{,}192$ cm^{-1}) ^1D state of atomic carbon, based on line positions and Einstein *A*-values from the Kurucz atomic database.[7] The ionization limit is near 1240 Å, so atomic carbon can be photoionized out of the ^1D state by H I 1215 Lyα, if there is sufficient collisional population of the level, a mere 1.3 eV above ground. There is a good match between the simulated C I recombination spectrum and many of the emission lines of α Cen A in the 1240–1248 Å interval, as well as with the emission patterns of Procyon, α Cen B, and α Boo. Cooler γ Cru, in contrast, displays a relatively weaker C I spectrum. Crucial to this study, one of the C I recombination lines enhances the red peak of Fe XII 1241 in both α Cen A and Procyon. However, the Fe XII profile of α Cen B appears to be much less affected.

Shaded vertical bands in the two panels highlight various incidental emission (and absorption) lines. The leftmost two absorptions in the left panel are Mg II ground-state transitions, prominent in the warm atmosphere of Procyon (although possibly interstellar), but also present in α Boo and γ Cru. The yellow shaded bands are for ground-state S I lines. The short-wavelength member of the pair is expected to be similar in strength to the more isolated long-wavelength component (a S I close blend). The latter appears in all the stars and, unlike C I, is similar in strength in the two red giants. Notably, the short-wavelength S I component enhances the blue peak of Fe XII 1241 in both α Cen A and Procyon. Again, the Fe XII profile of α Cen B appears less affected. The S I and C I blends in Fe XII 1241 of α Cen A and Procyon were overlooked in previous work, even though (in hindsight) the statistically significant twin peaks were clearly visible (e.g., Figure 5 and Figure C2(a) of A21).

In the right panel, prominent tan shaded emissions of the two red giants are Cr II transitions radiatively pumped by Lyα (e.g., Carpenter et al. 2018). However, no other fluorescent transitions (e.g., H_2, CO) are obvious. The Fe XII 1349 emission is weaker than 1241 (APED emissivities suggest $f_{1349}/f_{1241} \approx 0.57$), but apparently freer of extraneous blends.

5. FUV Analysis

The main aim of the FUV side of the analysis was to compare the Fe XII coronal lines with the corrected X-ray fluxes to test the HRC-I sensitivity decline discussed earlier.

[7] 1995 Atomic Line Data (R.L. Kurucz and B. Bell) Kurucz CD-ROM No. 23 (Cambridge, MA: Smithsonian Astrophysical Observatory).

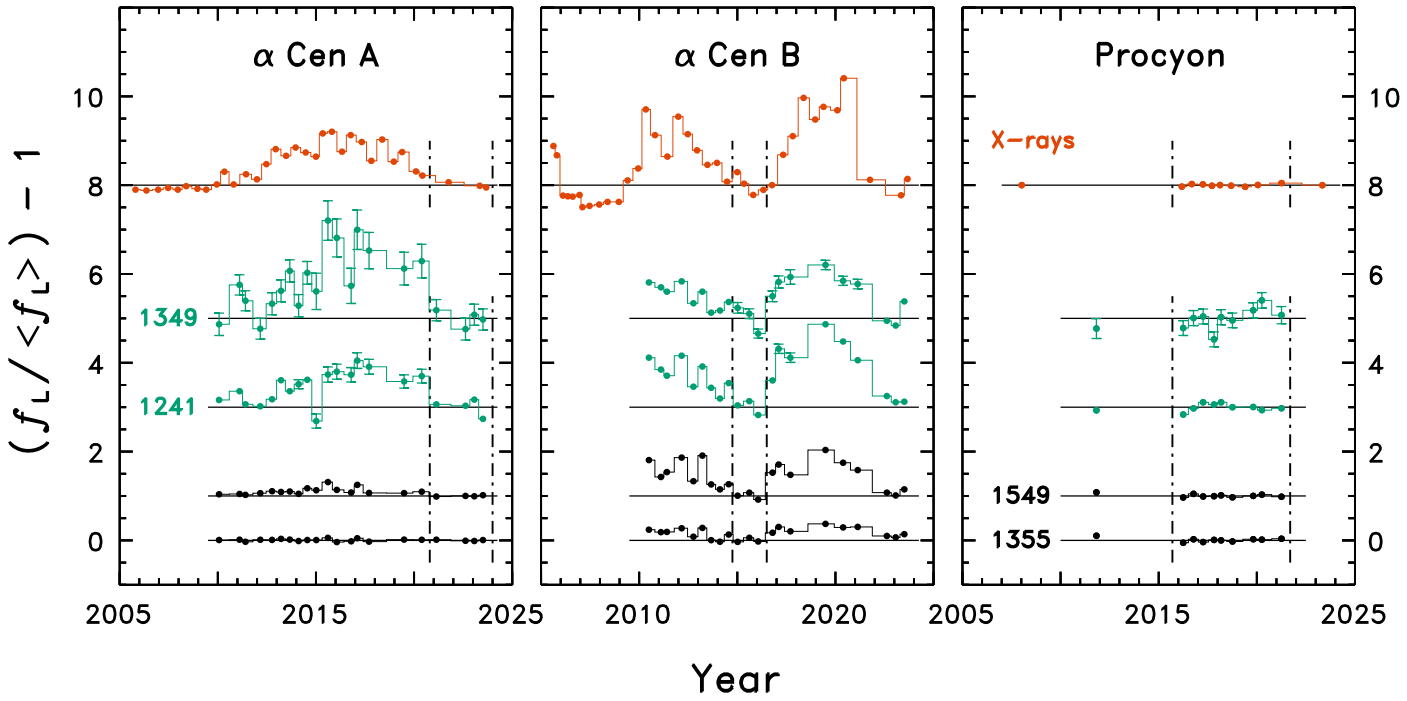

Figure 5. Differential light curves of α Cen AB and Procyon for high-S/N chromospheric and subcoronal emissions (black filled circles), the two Fe XII forbidden lines (green), and X-rays (red). Tracings are shifted vertically for clarity. Each time series was separately normalized to the average of the values between the vertical dashed lines. Horizontal lines mark the zero levels. Error bars of the weak Fe XII lines are shown explicitly for $(\sigma_L/ < f_L >) \geqslant 10$ %. "1355" refers to chromospheric O I; "1549" refers to subcoronal C IV.

Table 1
HST/STIS FUV Measurements of α Cen AB and Procyon: Epoch-average Spectra

Species	Wavelength (Å)	f_A	f_B (10^{-12} erg cm^{-2} s^{-1})	f_P
(1)	(2)	(3)	(4)	(5)
Fe XII	1241.985 ± 0.001[a]	0.0116 ± 0.0002[b]	0.0242 ± 0.0004	0.0268 ± 0.0008[b]
Fe XII	1349.396 ± 0.001[a]	0.0041 ± 0.0002[b]	0.0106 ± 0.0002	0.0078 ± 0.0010[b]
Cl I	1351.656[c]	0.127 ± 0.001	0.0503 ± 0.0004	0.474 ± 0.002
O I	1355.598[c]	0.193 ± 0.001	0.0788 ± 0.0005	0.361 ± 0.002
C IV	1548.204[d] + 1550.771[d]	2.93 ± 0.01	1.74 ± 0.01	9.13 ± 0.03

Notes. Unless otherwise noted, emission-line strengths (Cols. (3)–(5)) were from the pseudo-Gaussian modeling (AB22). Flux uncertainties were obtained from the fitting algorithm via a Monte Carlo scheme, or a quadratic sum of the bin-wise errors for the numerical integrations.
[a] Empirical values based on fitting the high-S/N α Cen B features.
[b] Derived from numerical integrations.
[c] Atomic Line List v3.00b4 (https://linelist.pa.uky.edu/newpage/).
[d] Ayres (2015).

This involved measuring line strengths in the individual time-domain FUV spectra, as well as the epoch averages, utilizing a "pseudo-Gaussian" fitting strategy (Gaussian exponent $\alpha = 2$ replaced by optimized α values). The approach, as well as motivations for it, was originally described by Ayres et al. (2021) for the Sun and by A21 and AB22 for other cool stars. In the present study, most of the FUV emissions were modeled with pseudo-Gaussians, although straight numerical integrations were applied to the faint, slightly distorted Fe XII profiles of α Cen A and Procyon. The spectra were registered in radial velocity (RV) according to two narrow chromospheric lines, Cl I 1351 and O I 1355.

Two representative transitions were measured in addition to the Fe XII pair: low-excitation, optically thin chromospheric O I 1355 (one of the velocity calibrators noted above, and likely formed by recombination in the Sun; Lin & Carlsson 2015), and high-excitation, optically thin, subcoronal C IV 1548 + 1550 (hereafter "1549"). The parameters that controlled the fitting algorithm were from Table 6 of A21. Examples of derived flux values are listed in Table 1, based on the epoch-average FUV spectra. Examples of the pseudo-Gaussian modeling for AB and Procyon can be found in A21.

Recalling that the APED f_{1349}/f_{1241} is 0.57, the empirical flux ratio of α Cen B in the high-S/N epoch-average spectrum is 0.44, based on the pseudo-Gaussian modeling (see, e.g., Figure C1(b) of A21). That suggests some contamination of the 1241 component if the theoretical value is correct. The empirical ratios of α Cen A and Procyon, for which the S I and C I blending is more severe, are even smaller: 0.35 and 0.29, respectively.

Incidentally, the Fe XII features of α Cen B—strong, symmetric, and nearly Gaussian—can be used to check the

forbidden-line wavelengths, which are challenging to measure in the laboratory. The NIST Atomic Spectra Database[8] lists "observed" wavelengths of 1242.00 and 1349.40 and "Ritz" values (from energy-level differences) of 1242.00 and 1349.36, with no explicit uncertainties cited.

The STIS epoch average of α Cen B is composed of various M and H echelle settings that have their own pipeline wavelength calibrations and additional post-facto corrections layered on top (see A21), so the coadded, epoch-average spectrum should achieve a high level of internal wavelength precision. The velocity zero-point was registered to the mean of the pair of narrow chromospheric Cl I and O I emissions noted earlier. That average is taken to represent the rest ("laboratory") frame of the star.[9] The wavelengths of the Fe XII transitions in that frame are 1241.985 ± 0.001 and 1349.396 ± 0.001, where the cited errors (about 0.1 H resel) were deduced from the pseudo-Gaussian modeling (AB22) and are larger than the statistical uncertainties associated with the zero-point correction. These empirical wavelengths are in good agreement with the NIST "observed" values, with the caveat that there is a potential systematic error of unknown size if the Fe XII forbidden lines display a nonnegligible disk-average Doppler shift, due to coronal velocity fields, which manages to survive the multiepoch averaging.

Measured fluxes of the three program stars are presented in Figure 5 as differential light curves, $(f_L / <f_L>) - 1$, where f_L is an integrated line strength (or 0.1–2.4 keV flux for the X-rays). The figure includes two FUV species (black filled circles: O I 1355 representing the 7000 K chromosphere, and C IV 1549 for the 10^5 K subcoronal layers); the 1.6 MK Fe XII forbidden lines (green filled circles: 1241 and 1349); and 1–3 MK X-rays (red filled circles). The X-rays were corrected for the proposed HRC-I post-2016 sensitivity decline. The STIS FUV M and H echelle modes have their own time-dependent radiometric calibrations, maintained by routine monitoring of UV-bright hot white dwarfs.

Each time series was separately normalized to the average of the values between the vertical dashed lines (the "$<f_L>$" above). The zero-points (horizontal lines) are shifted vertically for display purposes. The hot Fe XII forbidden lines exhibit large contrasts over the long-term starspot cycles of α Cen AB, comparable to that of coronal X-rays, and more substantial than the trends of the cooler diagnostics. The FUV coronal lines for the most part vindicate the corrected X-ray light curves: relatively constant time behavior for Procyon, but recent declines for both α Cen A and B to low levels commensurate with the respective historical cycle minima. The corroboration is in spite of the apparent blending contamination of Fe XII 1241 in α Cen A and Procyon (likely a relatively cycle-independent flux offset in both cases).

6. X-Rays + FUV

The final step was to scale the STIS Fe XII emissions of α Cen B in an effort to fill gaps in the coronal light curve (such as caused by the recent pause in HRC-I operations). Alpha Cen B has the advantage that its Fe XII 1241 feature appears to be much less affected by the contaminating S I and C I blends than α Cen A or Procyon. Helpfully, there are isolated S I and C I lines in the 1240–1250 Å interval (noted in Figure 4) that are predicted to be of similar strength to the blends in the Fe XII 1241 feature: S I 1247.13 + 1247.16 and C I 1243.79. The total strength of the S I and C I blend proxies in the FUV epoch average of B is 2.8×10^{-15} erg s^{-1}, about 12% of the Fe XII 1241 flux in that spectrum (Table 1). The contaminating chromospheric blends likely display only modest variability over the starspot cycle of B (like O I 1355 in Figure 5, which is a similarly weak chromospheric line and forms by recombination, as does C I 1241). Hence, a reasonable approximation is to assume that the blend contribution is fixed at the epoch average.

An Fe XII time series was constructed by adding the 1241 and 1349 fluxes and then subtracting the (assumed) constant blend contribution. Ratios of X-ray fluxes to blend-corrected Fe XII were based on temporal coincidences within $\pm$ 0.2 yr (a total of 15 pairs). The derived ratio was 525 $\pm$ 130 (35), where the parenthetical value is the standard error of the mean. The individual time-matched ratios displayed a large scatter, possibly bimodal, as a function of the corrected Fe XII flux, but no obvious trend with Fe XII. Much of the dispersion in the contemporaneous, though not simultaneous, data sets likely can be attributed to stochastic effects such as flares (the STIS data were not time-tagged, thus preventing application of a Chandra-like flare filter), active-region evolution, and rotational modulations (the spin period of B is 0.11 yr; AB22). Nevertheless, averaging the disparate values likely better approximates the hypothetical "instantaneous" X-ray/Fe XII flux ratio.

Figure 6 shows the result of interleaving the normalized X-ray luminosities (red filled circles) and scaled (according to the X-ray/Fe XII ratio above), blend-corrected Fe XII intensities (black filled circles) over the more limited time range, 2010–present, of the several consecutive joint Chandra/HST programs. Despite the scatter of the X-ray/Fe XII ratios of the sample, scaled Fe XII displays excellent coherence with the interspersed X-ray points. The agreement supports the original presumption that FUV Fe XII is a proxy for the coronal soft X-ray emission, not only for the specific case of α Cen B, but likely for other moderate-activity dwarfs whose EMDs also mimic the Fe XII emissivity curve.

The gray histogram tracing in Figure 6 is the full Chandra + XMM-Newton B time series advanced by 16 yr, demonstrating a roughly 8 yr period for the two cycles (and three peaks) collected so far during the post-ROSAT era. Counting ROSAT measurements from the 1990s, but Chandra and XMM-Newton pointings only through 2013.5, A14 reported a cycle duration of 19.2 ± 0.7 yr for A, based on a candidate peak in 1997–1999 (Figure 6 of A14), and 8.1 ± 0.2 yr for B. Now, with an additional decade of X-ray coverage, a clear second maximum is seen for A, 2015–2018, and a fourth for B, in 2019.5 (with an initial peak in 1995.5 during the ROSAT era; A14). The corresponding cycle period for A still is about 19 yr, consistent with the A14 estimate, but more reliable with the new peak bagged. (A rough error for the period is $\pm$1 yr arising from the uncertainty of centroiding the broad maxima; see A14.) The cycle period for B, based on the four peaks and their individual separations, is 8.0 ± 0.5 yr, similar to Figure 6 and the A14 conclusion.

Nevertheless the A period must be viewed in the context that only two peaks have been seen so far, the earlier one less well documented, and the fact that the several-century history of the sunspot cycle is replete with few-year variations around the

[8] https://physics.nist.gov/asd

[9] Notably, the influence of the gravitational redshift is eliminated, because it should be the same for the chromosphere and low corona.

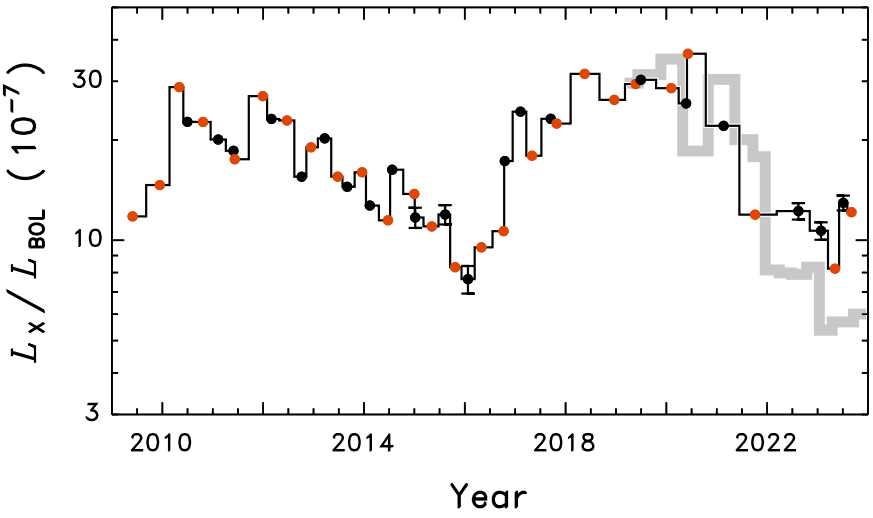

Figure 6. X-rays (red filled circles) plus scaled, blend-corrected Fe XII (black filled circles) of α Cen B over the span of the several joint Chandra/HST programs since SM4. Photometric uncertainty of the combined Fe XII flux is shown explicitly when larger than the symbol size ($\geqslant$5%). The gray curve is the Chandra/XMM-Newton X-ray time series advanced by 16 yr (two B cycles).

11 yr mean. The B period is more secure given that three full cycles have been witnessed, but the solar caveat concerning variable cycle lengths still holds. The clear differences in the cycle durations of A, B, and the Sun are all the more remarkable considering that the range in physical properties of the three dwarfs is small: the spread in masses is only $\pm 0.1\,M_{\odot}$, the rotation periods of A and the Sun are similar (B is $\approx$70 % longer), and the difference in ages probably is less than 1 Gyr (A09; AB22).

7. Discussion and Conclusions

The apparent FUV confirmation of the post-2016 decline of the HRC-I sensitivity was an unanticipated benefit of the HST part of the joint observing program. It is worth recalling that Chandra lacks viable calibrators for the soft spectral distributions of low-activity coronal stars like the Sun. Perhaps Procyon—and suitable F-type cousins—might be pressed into service for the purpose.

The FUV coronal forbidden lines have filled in parts of the α Cen B X-ray light curve where important epochs were missing, especially since 2021, when HRC-I was experiencing sporadic electronic issues. Curiously, the high-energy decline of B in 2010–2016 appears to have been smoother and shallower than the more abrupt recent drop in 2021–2023. The latter was similar to the equally precipitous cycle fall in 2005–2007, as illustrated in Figure 3 (see also the gray curve in Figure 6). Normally, the Sun displays a fast rise and slow decay in sunspot numbers (Hathaway et al. 1994) and also in X-rays, similar to the B cycle in 2008–2016. However, solar Cycle 24 (2009–2019) showed a steeper-than-normal decline (Figure 3), like that of the recent B behavior. The changing shapes of the high-energy light curves of the Sun and stars, as well as the slightly variable lengths of the solar sunspot cycle, emphasize that the dynamo is not a perfect machine, but rather has a somewhat chaotic aspect to its nature.

Given the similarities in the X-ray light curves of α Cen A and the Sun (aside from the longer duration and lower amplitude of the former), especially the equivalence in L_{MIN}/L_{BOL}, it is not a great leap of faith to imagine that A's low state is similarly devoid of starspots, while the high state also represents a larger coverage by dynamo-generated active regions, as on the Sun. The sensitivity corrections to the recent HRC-I CRs of A have yielded (so far) essentially the same global X-ray luminosity as seen during A's previous minimum. Constancy of coronal low states is a general characteristic of the high-energy solar cycles recorded over the past several decades and points to a suite of "basal" processes acting when sunspots are absent from the disk. As mentioned earlier, a key observational question is whether the coronal low states of a low-activity Sunlike star are immutable, or whether they might vary from cycle to cycle (the "Maunder Minimum" issue). The (albeit rather limited) evidence so far suggests that the low states truly are basal (hard lower limits).

In that regard, it is worth stressing that the Sun (and near-twin α Cen A) exists in a perhaps delicate condition, where starspots are present during the high phases of the cycle but mainly are absent during the low states. Many of the G-type dwarfs of the Sun's age likely share this condition. At the same time, the similarly old and more slowly rotating K dwarf of α Cen apparently is operating differently. Namely, the L_X/L_{BOL} levels of its several documented low states are comparable to the Sun's Cycle 24 maximum, and the B low states themselves apparently are variable (although, again, there are only a few examples so far). Both characteristics suggest that starspots still are plentiful during B's cycle minima, although they surge in numbers at the maxima, leading to a MAX/MIN contrast that, remarkably, is comparable to those of α Cen A or the Sun (Figure 3).

Then, there is the curious case of the F subgiant Procyon, which appears to be in a prolonged X-ray flat-line state, yet the level (in L_X/L_{BOL}) exceeds the maximum of the α Cen A cycle (and is similar to the MAX of solar Cycle 24). The nonsunspot, small-scale photospheric magnetic flux derives from near-surface convective turbulence (related to L_{BOL}, since the bulk of the stellar energy flux is carried by convection just below the visible layers). The bolometric normalization (L_X/L_{BOL}) should therefore compensate to some extent for the local-dynamo magnetic flux production among stars of different temperature (Procyon is about 800 K hotter than α Cen A and the Sun; α Cen B is about 600 K cooler than the two G stars). The conclusion is either that Procyon has a much more efficient small-scale dynamo than α Cen A or the Sun, leading to an

unusually high basal flux, or that Procyon is broadly covered by starspots, proliferating from a noncycling (or very long period) internal large-scale dynamo.

Relevant to this issue, Walter (1983) found that early/mid-F dwarfs surveyed by the pioneering Einstein X-ray Observatory (1978–1981) had high L_X/L_{BOL}, tended not to follow a rotation–activity connection (unlike the later F, G, and K dwarfs), and showed a relatively small dispersion of their normalized fluxes. These attributes point to an unusually efficient magnetic generation process (high L_X/L_{BOL}), which apparently is noncycling (low variance of L_X/L_{BOL}). Thus, as noted by Walter (see also A21), the nonsolar internal structure of the early/mid-F stars—a convective core, thick radiative envelope, and shallow convective layer at the surface—undoubtedly is playing a key role. Thus, Procyon offers a golden test case to challenge theoretical models of stellar dynamos (see, e.g., Charbonneau & Sokoloff 2023, and references to previous work therein).

Finally, and tangentially, the fact that both α Cen A and B will be near minimum activity for the next few years presents a favorable opportunity for Doppler-reflex campaigns aimed at detecting planetary companions. A candidate exoplanet around α Cen B was reported by Dumusque et al. (2012), based on HARPS RV measurements in 2008.4–2011.7, at a time when B was rising from a cycle MIN to a MAX. Subsequently, Hatzes (2013) and Rajpaul et al. (2016) argued that the inference of a planetary-like signature from the HARPS series could be affected by nuisance signals from chromospheric activity. Thus, the current epoch of dual minima of α Cen AB, combined with their steadily increasing separation on the sky (Figure 1), is an opportune time to carry out new RV planet searches on both binary components, with minimum activity interference on the search star and also minimum influence of scattered light from the star not being observed.

Acknowledgments

This work was based on observations from Chandra X-ray Observatory, processed at the Chandra X-ray Center, operated by the Smithsonian Astrophysical Observatory, under contract to NASA, and from Hubble Space Telescope, collected at the Space Telescope Science Institute, operated by the Associated Universities for Research in Astronomy, also under contract to NASA. The author thanks SAO and STScI for their grant support. The Chandra data sets described in this work can be accessed via Chandra Data Collection (CDC) 10.25574/cdc.162. HST FUV spectra were obtained from the Mikulski Archive for Space Telescopes at STScI in Baltimore, Maryland. These data sets can be found via https://doi.org/10.17909/a5em-ga92.

Appendix A
Chandra HRC-I X-Ray Measurements of α Cen AB and Procyon

The following two tables provide revised Chandra HRC-I X-ray measurements of α Cen AB and Procyon based on the simplified flare filter introduced earlier, and including a few more recent pointings than listed previously. ECFs were determined for each observation based on an EMD optimization scheme originally described by AB22.

Table A1
Chandra HRC-I Pointings: α Cen AB

ObsID	Date	t_{exp}	$(CR)_A$ (s)	$(CR)_B$ (s)	$(f_X)_A$	$(f_X)_B$
	(yr)	(ks)	(counts s^{-1})		(10^{-12} erg cm^{-2} s^{-1})	
(1)	(2)	(3)	(4)	(5)	(6)	(7)
6373	2005.805	5.15	0.44 (1)	2.22 (2)	3.4	16.0
6374	2006.362	5.11	0.43 (1)	0.98 (1)	3.4	7.2
6375	2006.960	2.67	0.44 (2)	1.02 (2)	3.4	7.5
7433	2007.469	5.04	0.46 (1)	0.69 (1)	3.6	5.1
7434	2007.961	5.11	0.44 (1)	0.73 (1)	3.4	5.4
8906	2008.389	10.08	0.48 (1)	0.81 (2)	3.7	6.0
8907	2008.961	9.34	0.45 (1)	0.81 (1)	3.5	6.0
9949	2009.409	10.06	0.44 (1)	1.46 (1)	3.4	10.6
9950	2009.949	10.05	0.50 (1)	1.82 (1)	3.9	13.2
10980	2010.335	9.76	0.65 (1)	3.61 (4)	5.0	25.9
10981	2010.808	10.03	0.50 (1)	2.83 (2)	3.9	20.4
12333	2011.437	4.88	0.62 (1)	2.18 (2)	4.8	15.7
12334	2011.993	10.07	0.56 (1)	3.39 (2)	4.3	24.3
14191	2012.473	10.10	0.74 (1)	2.86 (1)	5.6	20.6
14192	2012.950	10.06	0.92 (1)	2.37 (1)	6.9	17.1
14193	2013.480	10.59	0.84 (1)	1.93 (1)	6.4	14.0
14232	2013.963	10.05	0.94 (1)	1.99 (1)	7.1	14.4
14233	2014.477	9.62	0.88 (1)	1.42 (1)	6.6	10.3
14234	2014.999	10.11	0.83 (1)	1.71 (2)	6.3	12.4
16677	2015.346	10.07	1.11 (1)	1.36 (1)	8.3	9.9
16678	2015.810	10.08	1.13 (1)	1.02 (1)	8.4	7.5
16679	2016.330	10.03	0.88 (1)	1.16 (1)	6.7	8.6
16680	2016.771	10.01	1.06 (1)	1.28 (1)	8.1	9.6
16681	2017.335	9.99	0.96 (1)	2.13 (2)	7.6	16.1
16682	2017.823	10.00	0.73 (1)	2.62 (1)	5.9	20.1
20987	2018.378	5.12	0.95 (1)	3.63 (1)	7.8	28.4
21572	2018.967	5.11	0.69 (1)	2.96 (1)	5.9	23.7

Table A1
(Continued)

ObsID	Date	t_{exp}	$(CR)_A$ (s)	$(CR)_B$ (s)	$(f_X)_A$	$(f_X)_B$
	(yr)	(ks)	(counts s^{-1})		(10^{-12} erg cm^{-2} s^{-1})	
(1)	(2)	(3)	(4)	(5)	(6)	(7)
21573	2019.391	5.10	0.78 (1)	3.25 (1)	6.7	26.5
21574	2020.097	5.07	0.56 (1)	3.07 (1)	5.0	25.7
21575	2020.428	5.11	0.51 (1)	3.85 (4)	4.7	32.6
21576/7	2021.761	10.10	0.42 (1)	1.18 (1)	4.1	10.7
25497	2023.345	9.78	0.36 (1)	0.75 (1)	3.8	7.4
25498	2023.673	9.94	0.34 (1)	1.10 (1)	3.6	10.9

Note. Column (3): exposure times include dead-time corrections. Columns (4) and (5): A and B CRs were intensity-filtered to suppress flares, corrected for the 95% encircled energy of the $r = 1\farcs5$ detect cell, but not adjusted for the time-dependent sensitivity of HRC-I. Parenthetical value, s, is the (rounded) factor by which the standard deviation of all the time bins of a pointing exceeded the Poisson value for the flare-filtered average bin: values $\geqslant 2$ indicate significant volatility (mainly flares on component B). Columns (6) and (7): A and B flare-filtered X-ray fluxes (0.1–2.4 keV) at Earth were based on activity-dependent ECFs modeled for A and B separately (see AB22) and an assumed HRC-I sensitivity decline of 3.5% yr^{-1} since 2016. Formal Poisson uncertainties typically are 2% or less, due to the high CRs and long exposures. X-ray luminosities, L_X (10^{27} erg s^{-1}), can be obtained by multiplying Columns (6) and (7) by 0.214. Normalized X-ray fluxes, f_X/f_{BOL} (10^{-7}), or luminosities, L_X/L_{BOL} (10^{-7}), for α Cen A can be obtained by multiplying Column (6) by 0.368 and for B by multiplying Column (7) by 1.112.

Table A2
Chandra HRC-I Pointings: Procyon

ObsID	Date	t_{exp}	$(CR)_P$ (s)	$(f_X)_P$
	(yr)	(ks)	(counts s^{-1})	(10^{-12} erg cm^{-2} s^{-1})
(1)	(2)	(3)	(4)	(5)
8908	2008.020	4.78	1.51 (1)	11.1
18304	2016.183	9.68	1.45 (1)	10.7
18305	2016.685	10.06	1.51 (1)	11.3
18306	2017.254	10.03	1.47 (1)	11.3
18307	2017.713	9.95	1.40 (1)	10.9
18308	2018.128	9.99	1.40 (1)	11.1
18309	2018.692	9.76	1.35 (1)	10.9
21578	2019.406	5.01	1.28 (1)	10.6
21579	2020.051	5.07	1.30 (1)	11.1
21580	2021.261	5.09	1.29 (1)	11.6
25503	2023.341	2.87	1.12 (1)	11.0

Note. Columns are similar to those of Table 1. X-ray luminosities, L_X (10^{27} erg s^{-1}), can be obtained by multiplying Column (5) by 1.478. Normalized X-ray fluxes, f_X/f_{BOL} (10^{-7}), or luminosities, L_X/L_{BOL} (10^{-7}), can be obtained by multiplying Column (5) by 0.559.

Appendix B
Recent HST/STIS Observations of α Cen AB

Three STIS observations of α Cen AB were obtained subsequent to the A21 study of AB and Procyon. Unfortunately, there are no more recent STIS pointings on Procyon. The new AB visits were two orbits each, in the continuous viewing zone (avoiding Earth occultations). Initial target acquisition was of α Cen A, visually brighter of the pair, utilizing the STIS CDD and ND-filtered aperture F25ND5. The next observation, consisting of two 1900 s subexposures, was of A with the medium-resolution FUV echelle, E140M-1425 (1140–1729 Å), and the high-throughput $0\farcs2 \times 0\farcs2$ photometric slot. No peak-up was necessary, as the CCD centering is sufficiently accurate for that aperture. A deeper-than-normal 45 s E140M wavecal followed, to ensure adequate S/N in the face of fading lamp brightness. Then, a dispersed-light peak-up in the visible using CCD/G430M-4451 was performed with the $31'' \times 0\farcs05$ NDC ND-filtered long slit, to set up a 500 s NUV exposure of A with E230H-2713 (2578–2834 Å) and NDC, to record the important chromospheric Mg II 2796 + 2803 doublet. The ND-filtered long slit can be used for echelle observations of point sources and is needed to suppress the bright continuum of the G star to avoid a global CR (GCR) violation. That observation was followed by another nonstandard wavecal, E230H-2713, for 45 s. Next, the telescope was offset to α Cen B according to the known ephemeris. A second CCD/F25ND5 ACQ accurately centered B. Then, a dispersed-light peak-up with the $0\farcs2 \times 0\farcs09$ slit and CCD/G430M-3936 set up a 500 s E230H-2713 exposure of B. The GCR of cooler, NUV-dimmer B is safe for that combination of H CENWAVE and slit. A 45 s wavecal calibrated the E230M-2713 observation. Finally, an E140M echellegram of B was obtained with the photometric slot, in two subexposures of 1280 s, followed by another nonstandard FUV wavecal, to conclude the visit. The full observing scenario was described for completeness, but just the FUV exposures are listed in Table B1: the NUV spectra, although valuable for other purposes, are not germane to the present investigation.

Table B1
Recent HST/STIS Pointings on α Cen AB

Star	ObsID	Date	t_{exp}	S/N	RV
		(yr)	(s)	(resel^{-1})	(km s^{-1})
(1)	(2)	(3)	(4)	(5)	(6)
A	oeqw10010	2022.620	2 × 1900	13	−20.0
B	oeqw10040	2022.620	2 × 1280	7	−25.1
A	oeqw11010	2023.069	2 × 1900	13	−18.8
B	oeqw11040	2023.069	2 × 1280	7	−28.0
A	oevg10010	2023.510	2 × 1900	13	−20.2
B	oevg10040	2023.510	2 × 1280	7	−25.8

Note. All exposures were with E140M and the photometric slot. Column (3): observation date (UT). Column (4): exposure time. Column (5): a quality metric, the average S/N per resolution element (2 pixels). Column (6): the derived RV of the spectrum, based on a pair of narrow chromospheric lines.

ORCID iDs

Thomas Ayres https://orcid.org/0000-0002-1242-5124

References

Airapetian, V. S., Barnes, R., Cohen, O., et al. 2020, IJAsB, 19, 136
Akeson, R., Beichman, C., Kervella, P., et al. 2021, AJ, 162, 14
Ayres, T. R. 2009, ApJ, 696, 1931
Ayres, T. R. 2014, AJ, 147, 59
Ayres, T. R. 2015, AJ, 149, 58
Ayres, T. R. 2018, AJ, 156, 163
Ayres, T. R. 2021, ApJ, 923, 192
Ayres, T. 2022a, RNAAS, 6, 24
Ayres, T. R. 2022b, AJ, 163, 78
Ayres, T. 2023, ApJS, 266, 6
Ayres, T. R., Brown, A., Harper, G. M., et al. 2003, ApJ, 583, 963
Ayres, T., & Buzasi, D. 2022, ApJS, 263, 41
Ayres, T., De Pontieu, B., & Testa, P. 2021, ApJ, 916, 36
Babcock, H. W. 1961, ApJ, 133, 572
Carlsson, M., & Stein, R. F. 1992, ApJL, 397, L59
Carpenter, K. G., Nielsen, K. E., Kober, G. V., et al. 2018, ApJ, 869, 157
Charbonneau, P., & Sokoloff, D. 2023, SSRv, 219, 35
Dumusque, X., Pepe, F., Lovis, C., et al. 2012, Natur, 491, 207
Eddy, J. A. 1976, Sci, 192, 1189
Hathaway, D. H., Wilson, R. M., & Reichmann, E. J. 1994, SoPh, 151, 177
Hatzes, A. P. 2013, ApJ, 770, 133
Judge, P. G., Lockwood, G. W., Radick, R. R., et al. 2012, A&A, 544, A88
Leighton, R. B. 1969, ApJ, 156, 1
Lin, H.-H., & Carlsson, M. 2015, ApJ, 813, 34
Liu, H.-L., Rempel, M., Danabasoglu, G., et al. 2023, JGRD, 128, e2022JD037626
Parker, E. N. 1970, ApJ, 162, 665
Rajpaul, V., Aigrain, S., & Roberts, S. 2016, MNRAS, 456, L6
Rempel, M., Bhatia, T., Bellot Rubio, L., et al. 2023, SSRv, 219, 36
Robrade, J., Schmitt, J. H. M. M., & Favata, F. 2005, A&A, 442, 315
Robrade, J., Schmitt, J. H. M. M., & Favata, F. 2012, A&A, 543, A84
Rutten, R. J., & Uitenbroek, H. 1991, SoPh, 134, 15
Schmitt, J. H. M. M., & Liefke, C. 2004, A&A, 417, 651
Walter, F. M. 1983, ApJ, 274, 794
Wilson, O. C. 1978, ApJ, 226, 379
Wood, B. E., Laming, J. M., Warren, H. P., et al. 2018, ApJ, 862, 66
Yeo, K. L., Solanki, S. K., Krivova, N. A., et al. 2020, GeoRL, 47, e90243